Accuracy of heart strain rate calculation derived from Doppler tissue velocity data

A Santos[1], MJ Ledesma-Carbayo[1], N Malpica[1-3], M Desco[2], JC Antoranz[3], P Marcos-Alberca[2], MA Garcia-Fernandez[2].

[1] Universidad Politecnica de Madrid, E-28040 Madrid, Spain.
[2] Hospital General Universitario 'G. Marañón', E-28007 Madrid, Spain.
[3] Universidad Nacional de Educación a Distancia, E-28040 Madrid, Spain.

ABSTRACT

Strain Rate (SR) Imaging is a recent imaging technique that provides information about regional myocardial deformation by measuring local compression and expansion rates. SR can be obtained by calculating the local in-plane velocity gradients along the ultrasound beam from Doppler Tissue velocity data. However, SR calculations are very dependent on the image noise and artifacts, and different calculation algorithms may provide inconsistent results. This paper compares techniques to calculate SR.

2D Doppler Tissue Images (DTI) are acquired with an Acuson Sequoia scanner. Noise was measured with the aid of a rotating phantom. Processing is performed on polar coordinates. For each image, after removal of 'black spot' artifacts by a selective median filter, two different SR calculation methods have been implemented. In the first one, SR is computed as the discrete velocity derivative, and noise is reduced with a variable-width gaussian filter. In the second method a smoothing cubic spline is calculated for every scan line according to the noise level and the derivative is obtained from an analytical expression.

Both methods have been tested with DTI data from synthetic phantoms and normal volunteers. Results show that noise characteristics, border effects and the adequate scale are critical to obtain meaningful results.

Keywords: Strain Rate, Doppler, Cardiac Ultrasound, DTI, heart, velocity gradient, spline, myocardium

1. INTRODUCTION

Current clinical methods for evaluation of cardiac function by echocardiography are mainly qualitative or semiquantitative. One of the most commonly used is the qualitative assessment of regional myocardial motion and deformation. Several new techniques have been proposed to provide quantitative motion information, such as the analysis of endocardial border displacement and the recently introduced Doppler Tissue Imaging (DTI) technique. This new imaging modality allows for the measurement of velocities at any point in the ventricular wall during the cardiac cycle, providing information about subtle wall motion abnormalities which are difficult to observe just by visual analysis [1-3]. Several studies have been carried out to determine normal values of myocardial velocities and to show its sensitivity to detect wall motion abnormalities in several pathologies [4-7].

However, tissue velocities represent both local contractile and elastic properties and whole heart translation movement and tethering effects. In order to separate local and global effects a new parameter called 'Strain Rate' has been proposed to measure the local contraction and deformation. Ultrasound strain rate has recently been introduced by Heimdal et al. [8] and preliminary studies have been carried out to evaluate its precision and clinical use [9, 10]. Strain Rate Imaging can be obtained by calculating the local in-plane velocity gradients along the ultrasound beam from Doppler Tissue velocity data. However, Strain Rate calculations are very dependent on the image noise and artifacts, and different calculation algorithms may provide inconsistent results.

This paper stresses the importance of considering noise and artifacts characteristics in the Strain Rate calculation method. Several calculation methods are compared taking into account real DTI noise characteristics measured with the aid of a rotating phantom. According to this model, the performance of two strain rate calculation methods is assessed. Analysis is performed on both synthetic phantom and real images acquired from normal volunteers.

2. DEFINITIONS

2.1. Strain

The strain-stress relationship is a common concept used to investigate the mechanical properties of materials and has recently been applied to the analysis of cardiac tissue properties. The concept of strain (ε) corresponds to the deformation of an object as a function of an applied force stress (s). It represents the percentage of change of the unstressed dimension after the application of stress, and holds for both expansion (positive strains) and compression (negative strains) [8, 11]. Considering a one-dimensional object, the possible stress deformations are lengthening and shortening. In this case the strain can be expressed as the difference between the original length (L_0) and the length (L) after deformation, normalized by the original length (L_0), as shown in the following equation:

$$\varepsilon = \frac{L - L_0}{L_0} \tag{1}$$

As shown, the strain is a dimensionless parameter and, by convention, positive strains correspond to lengthening and negative strains to shortening.

In some cases the length of the object is known during the deformation process, in that case we can define the instantaneous strain as:

$$\varepsilon(t) = \frac{L(t) - L(t_0)}{L(t_0)} \tag{2}$$

where ($L(t)$) is the length at a given instant (t) and ($L(t_0)$) is the original length. When this relative measure is referred to the original length ($L_0 \equiv L(t_0)$) the strain corresponds to the *Lagrangian strain*. But we could also express the deformation relative to the length at the previous instant. This definition is known as *natural* or *Eulerian strain* and can be expressed by:

$$d\varepsilon_N(t) = \frac{L(t + dt) - L(t)}{L(t)} = \frac{dL}{L(t)} \tag{3}$$

where $d\varepsilon_N(t)$ is the amount of deformation occurring in a infinitesimally small time interval dt. Integrating through the whole time interval we get the total strain that has occurred. A relationship between the two definitions is found for the case of constant deformation rate as shown in the following expressions:

$$\varepsilon_N(t) = \ln(1 + \varepsilon(t)) \longleftrightarrow \varepsilon(t) = \exp(\varepsilon_N(t)) - 1 \tag{4}$$

It has been shown that natural strain is more adequate for the cardiac application because is not influenced by the initial time and length definitions [11].

All the definitions expressed for the one dimensional case can be generalized for two and three dimensions leading to the so called *strain tensor*, as a function of time with both the Lagrangian and the natural forms [10]. For the case of two dimensions the strain tensor corresponds to:

$$\begin{bmatrix} \varepsilon_x & \varepsilon_{xy} \\ \varepsilon_{yx} & \varepsilon_y \end{bmatrix} \quad \textit{with} \quad \begin{cases} \varepsilon_x = \dfrac{\Delta x}{x} & \varepsilon_{xy} = \dfrac{\Delta x}{y} \\ \varepsilon_{yx} = \dfrac{\Delta y}{x} & \varepsilon_y = \dfrac{\Delta y}{y} \end{cases} \tag{5}$$

where ε_x and ε_y are the two normal strains, and ε_{xy} and ε_{yx} are the two shear strains.

2.2. Strain Rate

The strain rate is a measurement of the rate of deformation and corresponds to the velocity of the deformation process. Taking into account equations (1) and (2) and the latter definition, the instantaneous strain rate $\varepsilon(t)$ is expressed as the temporal strain derivative:

$$\varepsilon(t) \equiv \frac{d\varepsilon(t)}{dt} = \frac{dL(t)}{dt} \cdot \frac{1}{L(t)} = \frac{L'(t)}{L(t)} \tag{6}$$

with $L'(t)$ being the rate of deformation and $L(t)$ the instantaneous length. The strain rate units are s^{-1}, compared with the rate of deformation units m·s^{-1}. Both Eulerian and Lagrangian strain rates can be defined, and analogous expressions are found for the two and three dimensional *strain rate tensors*.

As a conclusion, both strain and strain rate are closely related and they can be derived one from each other as we will discuss later.

3. PREVIOUS STUDIES

Different approaches have been proposed to calculate the strain and strain rate parameters; some preliminary studies have been carried out to evaluate their precision and clinical usefulness [8-10]. Two main methods have been proposed: the Cross-correlation method and the velocity gradient method.

The Cross-correlation method is based on the principles of elastography where two consecutive radiofrequency signals are compared to extract information about the tissue elasticity properties [12, 13]. Considering two consecutive radiofrequency signals applied to a tissue under deformation, the resultant backscatter signals received have similar patterns, except for a temporal shift related to the actual deformation. Cross-correlation analysis provides the temporal shift or delay introduced due to the object motion. From this analysis, different parameters such as the change in distance, local motion, velocities, etc., can be derived. The principal limitation of this technique is its high computational cost and the need of very high temporal resolution to avoid noisy estimates. That limits its application to M-mode acquisition.

On the other hand, Fleming et al.[14] and Uematsu et al.[15] introduced the concept of myocardial velocity gradient as an indicator of local contraction and relaxation. This concept is directly related to the already formulated Eulerian strain rate parameter (6) under the assumption of linear and uniform strain (homogeneous, isotropic and incompressible material) as can be shown in the following expression:

$$\varepsilon(t) \equiv \frac{d\varepsilon(t)}{dt} = \frac{dL(t)}{dt} \cdot \frac{1}{L(t)} = \frac{L'(t)}{L(t)} \approx \frac{v_1(t) - v_2(t)}{L(t)} \tag{7}$$

where $v_1(t)$ and $v_2(t)$ are the local instantaneous velocities at two myocardial points separated an $L(t)$ distance. This formulation allows to compute myocardial strain rate as the spatial gradient of myocardial velocities, which can be obtained by Doppler echocardiography. Since the computational load is not high it can be implemented as a post-processing step after acquiring Doppler Tissue images or in real-time from digitally stored tissue velocity information [8]. The axial natural strain component can be calculated from the strain rate curve time-integration expressed by:

$$\varepsilon_N(t) = \int_{t_1}^{t} \dot{\varepsilon}_N(t)\, dt \qquad (8)$$

Preliminary normal and pathological values of strain and strain rate have been investigated with this method in 2D sequences [9, 16, 17]. Its practical clinical use is still under research.

A limitation of all ultrasonic methods is that only the axial component can be computed. Another limitation of both techniques is their sensitivity to noise and artifacts present in the signals or images, that hamper the numerical calculation of the gradient. Numerical gradients are very sensitive to noise and good results are only obtained when smoothing is applied, limiting the spatial resolution of the method. In the following sections the problem of sensitivity to noise is considered, in order to obtain good strain rate estimates from the velocity gradient of DTI images, keeping the best possible spatial resolution and taking into account the characteristics of noise and artifacts.

4. MATERIAL AND METHODS

Noise and artifacts in DTI images were characterized using a rotating phantom. The conclusions are applied to the strain rate calculation methods. A preprocessing step and two new strain rate (SR) calculation methods are proposed. In the first one, SR is computed as the discrete velocity derivative, and noise is reduced with a variable-width gaussian filter. In the second method a smoothing cubic spline is calculated for every scan line according to the noise level and the derivative is obtained from an analytical expression. Performance of the two methods is quantitatively compared on data from a synthetic phantom and demonstrated on normal volunteers.

4.1. Noise characterization and filtering

A previous study was carried out to characterize noise and artifacts in the image using a rotating phantom, as described by Fleming [14]. A diagram of the phantom is shown in **Figure 1**. A DC motor produces a controlled rotation of a cylindrical sponge immersed in a water tank. A stroboscopic lamp is used to calibrate the system in order to produce the desired angular velocity. Values with similar amplitude to the cardiac velocity (1-5 cm/s) were chosen. The angular velocity is known at every moment, so the axial component of the velocity can be calculated at every point in the sponge, allowing to calculate the theoretical DTI image.
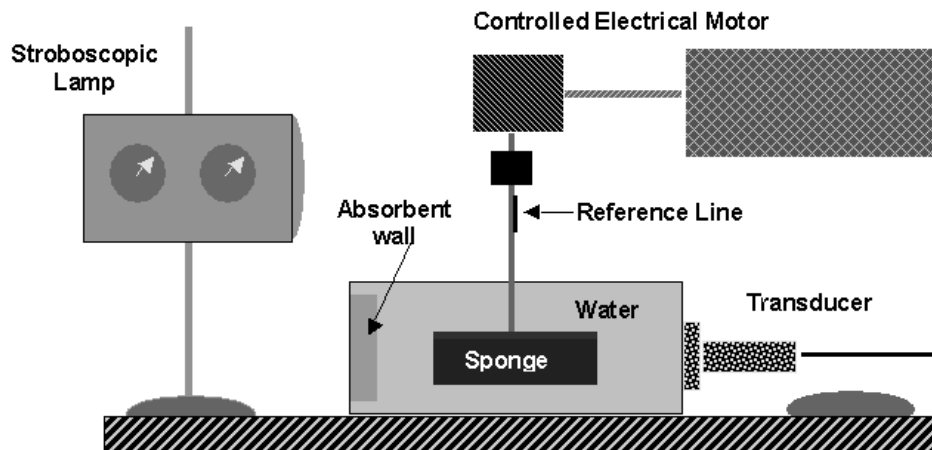

Figure 1. Diagram of the rotating phantom.

Phantom DTI images were acquired with an Acuson Sequoia® scanner (Mountain View, CA, USA) using different color calibration tables and system parameters. The difference between the ideal calculated image and the acquired image was studied in polar coordinates (**Figure 2**). Two different sources of error were identified: an additive random noise and the presence of 'black spot' artifacts, usually small in size, which do not actually correspond to low velocities.
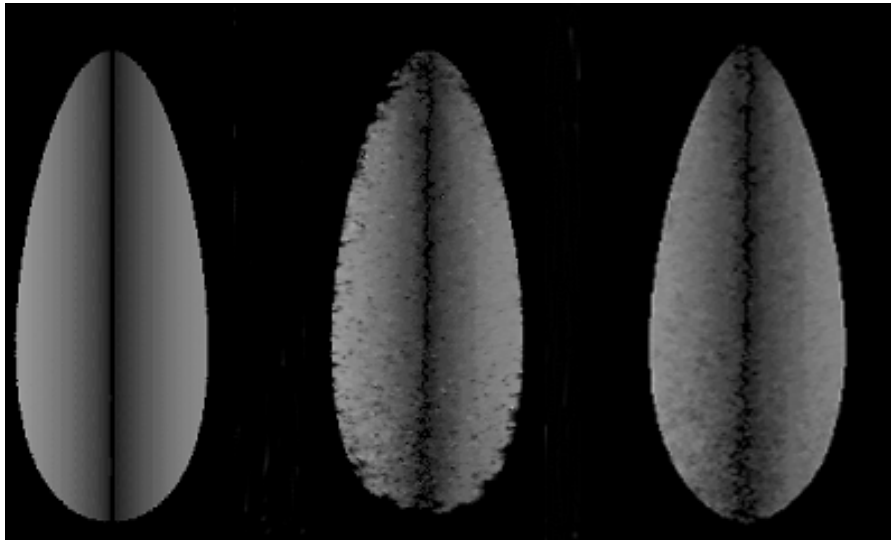
Figure 2. Phantom images in polar coordinates (from left to right): theoretical, acquired and corrected.

As a result, the random noise was characterized as a leptokurtic distribution with a standard deviation of 2% of the velocity span. Another important conclusion of this study was the influence of the different color tables on the analysis. The accuracy in obtaining velocity information by decoding the color is different for each table and also for different parts of the same table.

Another effect that appears on the images is the existence of some blurring at the edges. It is due to several causes that limit the resolution of the scanner itself, plus the effect of the interpolation when converting from polar to Cartesian coordinates to generate the image. To avoid this problem when characterizing the noise, an eroded mask of valid velocities (higher than a threshold) was applied.

A specific filter was designed to eliminate 'black–spot' artifact by means of a selective median filter. Other authors have already proposed median filtering for noise suppression in ultrasound images [18]. Our approach consists of a median filter only applied where artifacts are present and consequently not affecting the signal level at other points. This increases significantly the signal to noise ratio. Artifacts are identified as those areas, of the appropriate size, where the difference between the original and the median-filtered images is higher than a threshold obtained from the random noise distribution (2σ). **Figure 2** shows the result of the artifact-correction filter.

4.2. Strain Rate Synthetic Phantom

A synthetic phantom was designed to test the different strain rate algorithms. The phantom is an image consisting of a ramp of continuously increasing velocity with value range and gradient similar to those found in real cardiac images. Different disturbing effects can be independently added to study their influence in the algorithm performance. These effects are:

1. Black spot artifacts of different sizes.
2. Interruption of the ramp to simulate heart wall borders.
3. Blurring at the borders, modeled as a gaussian smoothing.
4. Additive noise with the statistical properties found in the previous study.

This phantom was used to assess and compare the performance and robustness of the two algorithms described below with respect to the different disturbing effects. **Figure 3** shows the synthetic phantom image, with all the disturbing effects added. On the right part, the ideal profile and the profile with all the effects are displayed.
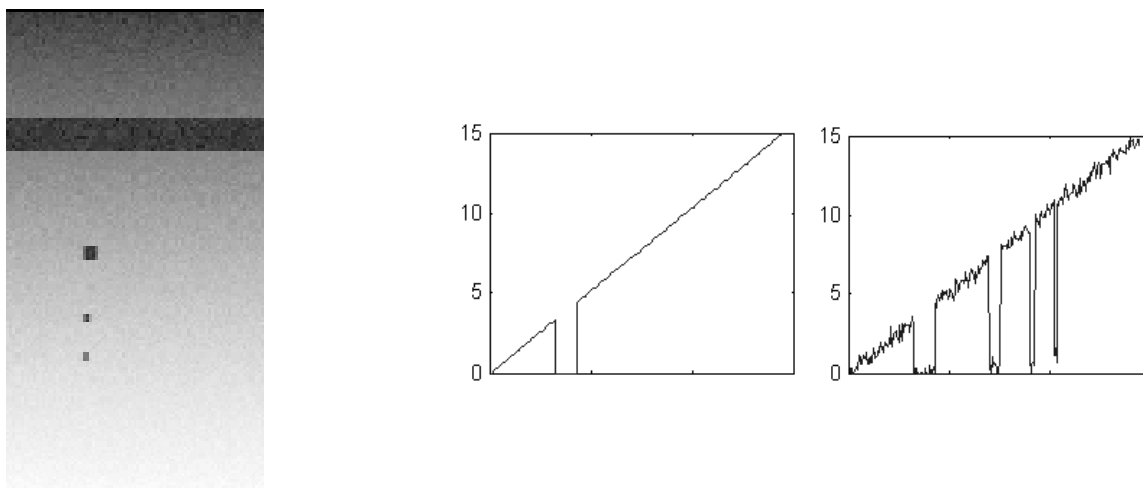
Figure 3. Left: synthetic phantom image. Middle: ideal profile. Right: profile with realistic distortions.

4.3. Strain Rate Calculation methods

Most of the published literature on strain rate imaging does not include detailed explanations on the method used to calculate the strain rate [8-10]. In broad terms, they consist of a smoothing step (averaging) for noise reduction, followed by a discrete gradient calculation using points separated a given distance (usually 1 or 0.5 cm). The main limitation of this approach is the low spatial resolution achieved. Averaging at the borders, due to the already mentioned blurring effect, results in very high values of spatial gradient at the edges, specially critical when transmural gradient is being calculated.

In this section two new procedures are proposed to compute the velocity gradient avoiding the edge effects as much as possible. Experiments were also carried out to find the spatial resolution obtained for a reasonable signal-to-noise ratio. In both methods the derivative is calculated along the direction of the ultrasound beam (ρ) by converting the image into polar coordinates.

The selective median filter explained in 4.1 is applied. In order to avoid the edge blurring effect, a morphological erosion is applied before calculating the strain rate.

Adaptive Discrete Algorithm

The first method is similar to the one proposed by Heimdal et al. [8, 13]. Averaging is applied along each line in the polar image, followed by the calculation of the gradient as the difference between points separated a distance s. Both averaging and gradient scope are adjusted when approaching the wall edges, in order not to include in the calculations points outside the wall.

Cubic smoothing spline algorithm

The second method proposed is based on a piece-wise cubic spline smoothing. For every scan line intervals with valid velocity values are identified and a cubic smoothing spline is fitted in each interval. This procedure provides a continuous framework allowing for an analytical calculation of the derivative at each point. Smoothing splines are analyzed in detail in [19], many other authors have proposed extensions and applications [20, 21]. This method consist of a interpolation process with a relaxed constraint in order to achieve an approximate fit instead of the perfect fit obtained with traditional interpolation. The formulation for cubic splines is expressed by:

$$p\sum_i (f(k) - s(k))^2 + (1-p)\int (s^2(x))^2 dx \qquad (8)$$

where p is the regularization parameter, that represents the tuning factor to filter the noise. Reinsch[19] proposed an automatic method to calculate the regularization parameter when noise variance was known, however the restriction imposed by the calculation of the derivative is stronger than the one imposed to get a reasonable signal to noise ration when smoothing splines are used only for filtering purposes.

4.4. Experimental setting

The two proposed methods are compared using the synthetic phantom described in 4.2. Spatial resolution is assessed by measuring the resulting FWHM for every method. Since theoretical strain rate values are known the mean square error can be calculated. Sensitivity to the disturbing effects is also analyzed.

Real DTI studies with normal volunteers were acquired on an ACUSON Sequoia scanner (Mountain View, CA, USA) and later transferred to a PC by a magnetic optical disk in DICOM format. Strain rate images were calculated using the best algorithm parameters as obtained from the phantom simulations.

5. RESULTS

In a first step the two algorithms were characterized to find the proper settings that produce equivalent spatial resolution. Resultant FWHM of the filters was calculated for this purpose. **Figure 4** illustrates how an FWHM of 0.8 cm. (cubic spline smoothing algorithm, p=0.001) was found to be equivalent to s=0.8 cm for the adaptive discrete algorithm.
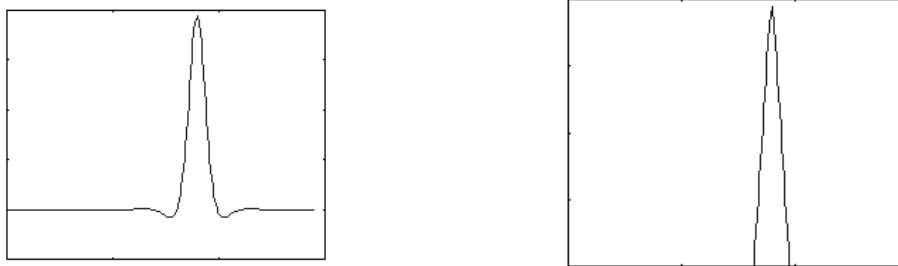

Figure 4. Measured FWHM. FWHM = 0.8 cm. Left: cubic spline smoothing algorithm, p=0.001. Right: adaptive discrete algorithm, s= 0.8 cm.

Once equivalent spatial resolution settings were found, the two algorithms were compared in the presence of noise varying the FWHM. The mean square error (MSE) with respect to the ideal strain rate was calculated for different FWHM with both algorithms as shown in **Table 1**. **Figure 5** shows strain rate profiles resultant from the two algorithms at different spatial resolutions (FWHM).

Table 1. Mean Square Error (MSE) of Strain Rate at different FWHM.

Algorithm	FWHM= 1cm	FWHM= 0.8 cm	FWHM= 0.5 cm	FWHM= 0.3 cm
Cubic Smoothig Spline	0.0120 (p = 0.0005)	0.0180 (p = 0.001)	0.0552 (p = 0.005)	0.2473 (p = 0.05)
Adaptive Length Discrete	0.0132 (s = 1cm)	0.0215 (s = 0.8cm)	0.0731 (s = 0.5cm)	0.2815 (s = 0.3cm)

We conclude that both methods give similar mean square error at the same spatial resolution, with slightly better results for the cubic spline smoothing algorithm. The experiments have been performed for FWHM from 1 cm to 3 mm, although the mean square error is very high for resolutions better than 5 mm. This limitation means that good results for transmural strain rate can hardly be obtained if the image characteristics are not improved.
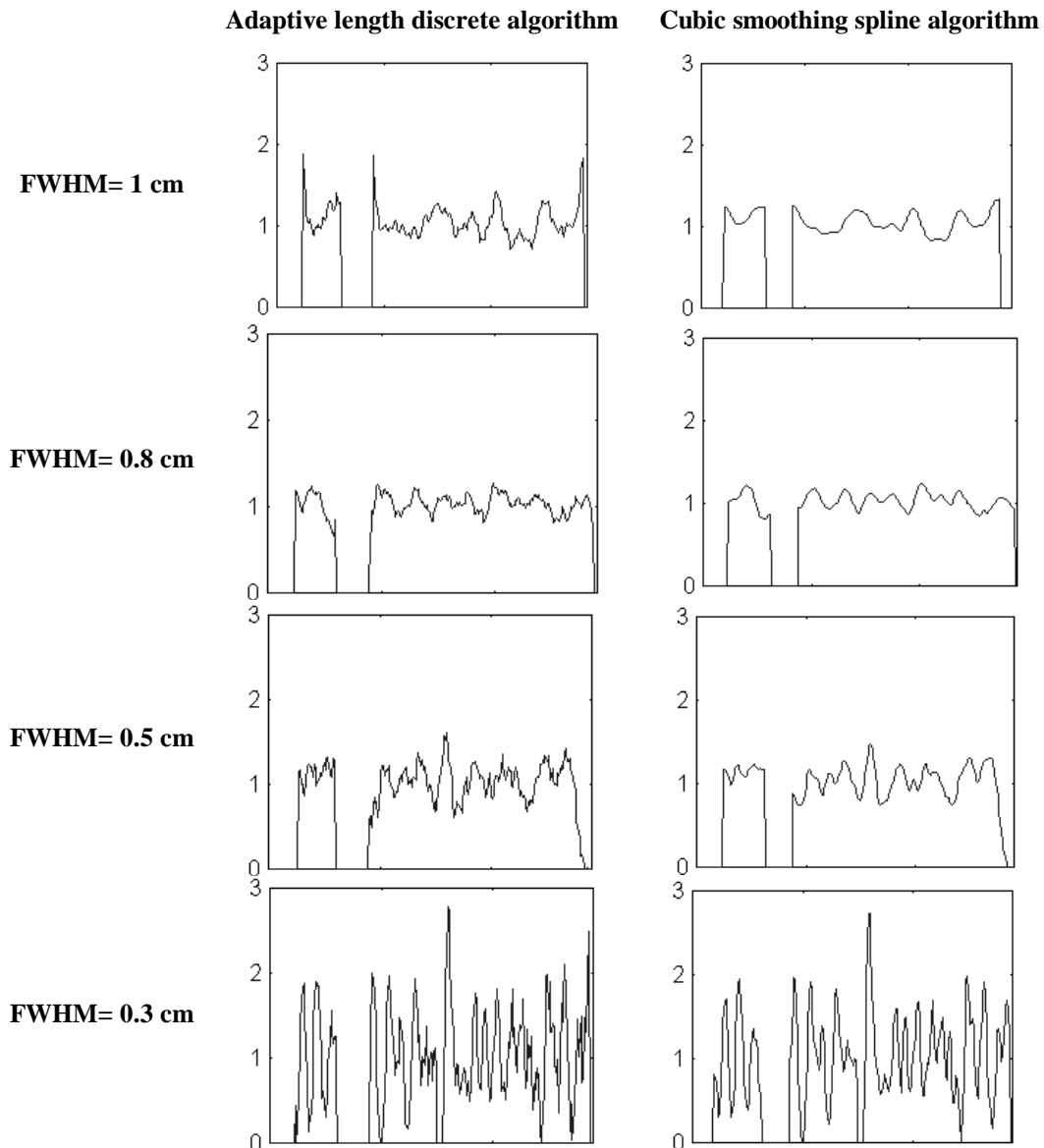

Figure 5. Strain Rate profiles for both algorithms at different values of FWHM.

The effect of the preprocessing steps was also evaluated. **Figure 6** shows the result of the two algorithms with and without black spot correction. FWHM of 0.8 cm. was chosen for these experiments.
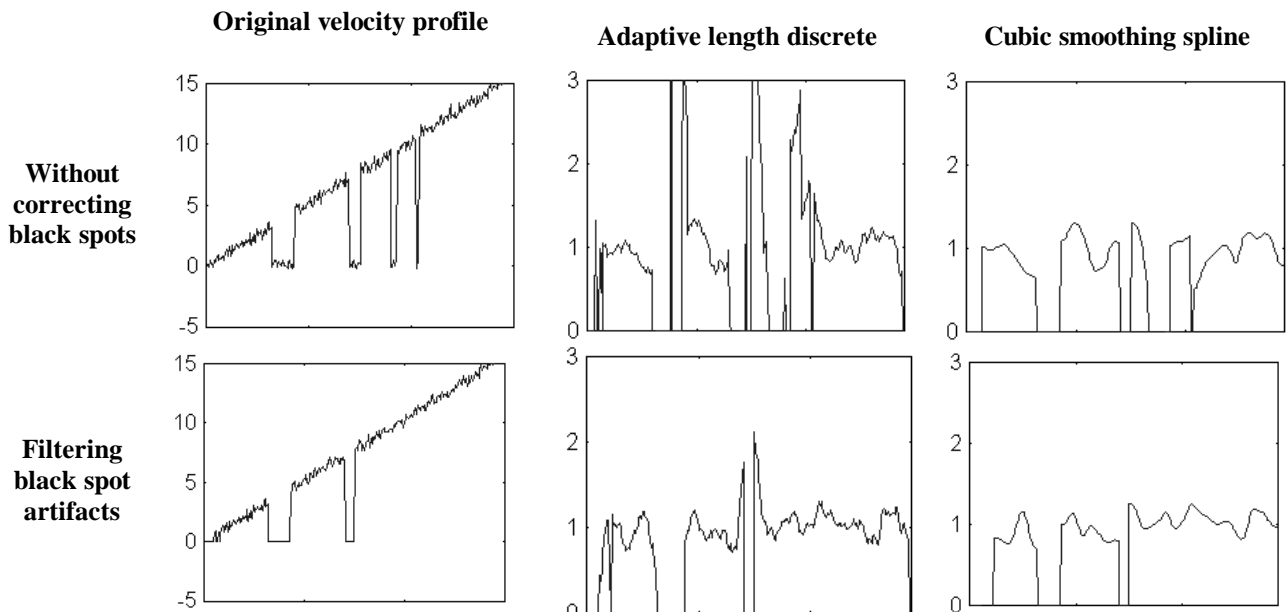
Original velocity profile   **Adaptive length discrete**   **Cubic smoothing spline**

Figure 6. Left. Original velocity profile. Middle and Right. Strain Rate profiles provided by both algorithms with and without black spot correction.

Influence of the edge blurring was also considered. **Figure 7** illustrates the performance of the two algorithms using or not border erosion, for FWHM of 0.8 cm.
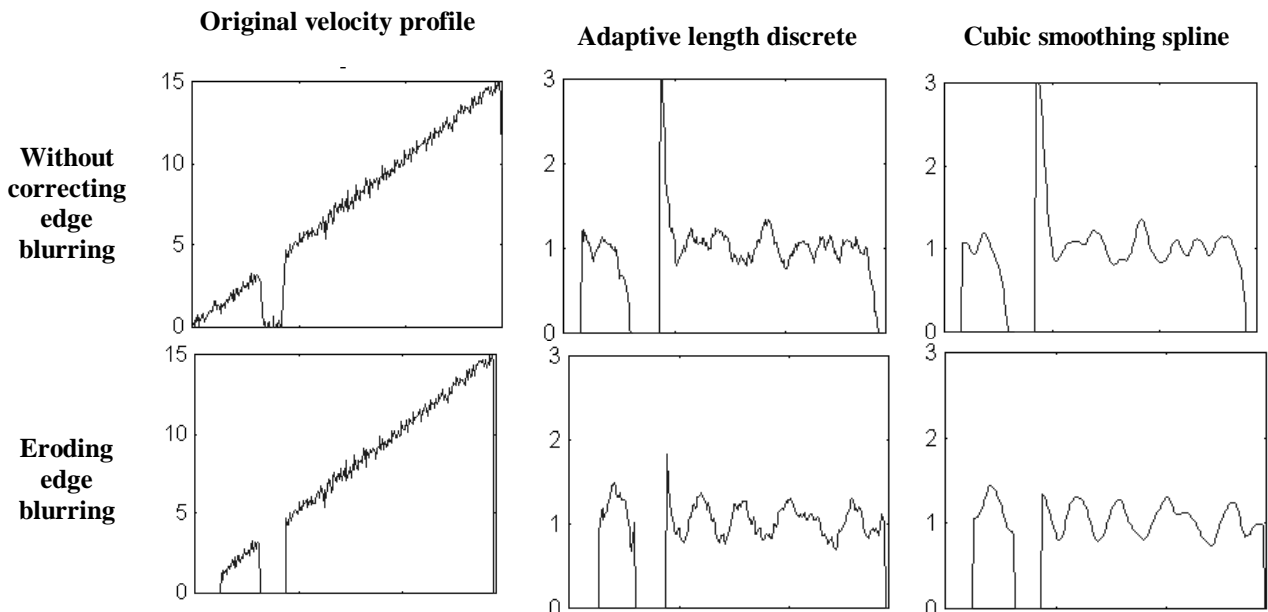
Original velocity profile   **Adaptive length discrete**   **Cubic smoothing spline**

Figure 7. Left. Original velocity profile. Middle and Right. Strain Rate profiles from both algorithms with and without edge blurring erosion.

It seems that the cubic smoothing spline algorithm is clearly more robust in the presence of 'black spots' artifacts. However, the effect of the edge blurring is enormous at the wall borders for both algorithms. As a conclusion, an improvement of the preprocessing steps is clearly demanded since erroneous results may arise when no corrective measurements are taken.

The best configuration of the described algorithms was also tested on real DTI images from normal volunteers. Four chambers view images were carefully acquired to have the cardiac wall along the ultrasound beam to get the pure longitudinal natural strain rate component from the strain rate analysis. Paresternal long-axis views were also carefully acquired to have the cardiac wall perpendicular to the ultrasound beam to be sure that the pure radial (transmural) natural strain rate component is being calculated. In **Figure 8** the original velocity image and the resultant strain rate image are shown.
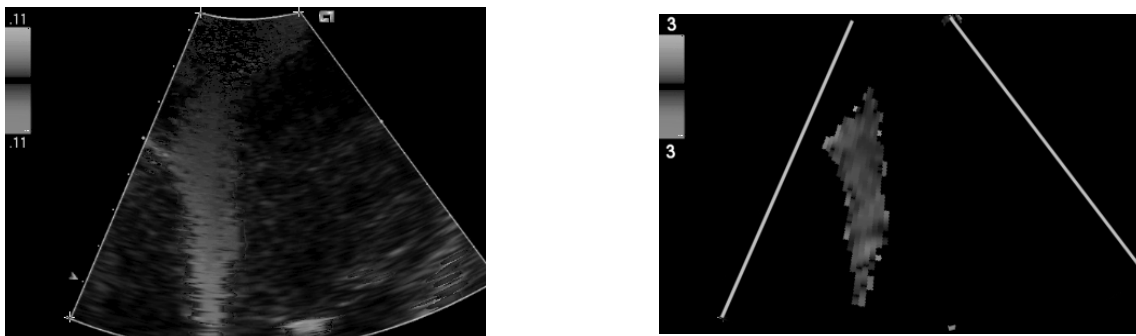

Figure 8. Left. Original velocity image. Right. Strain Rate image.

6. CONCLUSION

This paper reviews some factors that affect the calculation of strain rate images from Doppler Tissue data. Two methods to calculate the strain rate are proposed and evaluated. The effect of noise and artifacts have been shown to be critical to obtain meaningful results and the algorithms are very sensitive when no corrections are applied. Scale has also been studied and it has been shown that at resolutions better than 5 mm the strain rate cannot be calculated with a reasonable accuracy. To conclude, we consider that Strain Rate calculation is very sensitive to the image quality, being its clinical use still under discussion.

REFERENCES

1. K. Miyatake, M. Yamagishi, N. Tanaka, M. Uematsu, N. Yamazaki, Y. Mine, A. Sano, and M. Hirama, "New method for evaluating left ventricular wall motion by color-coded tissue Doppler imaging: in vitro and in vivo studies," *J Am Coll Cardiol*, vol. 25, pp. 717-24, 1995.
2. M. A. García-Fernández, J. L. Zamorano, and J. Azevedo, *Doppler Tissue Imaging*. New York: McGraw-Hill, 1997.
3. M. Desco, C. Antoranz, and M. A. García-Fernández, "Quantitative analysis of colour-coded Doppler tissue images.," presented at *Computer Assisted Radiology CAR'96*, Amsterdam, 1996.
4. C. L. Donovan, W. F. Armstrong, and D. S. Bach, "Quantitative Doppler tissue imaging of the left ventricular myocardium: validation in normal subjects," *Am Heart J*, vol. 130, pp. 100-4, 1995.
5. J. Gorcsan, 3rd, D. P. Strum, W. A. Mandarino, V. K. Gulati, and M. R. Pinsky, "Quantitative assessment of alterations in regional left ventricular contractility with color-coded tissue Doppler echocardiography. Comparison with sonomicrometry and pressure-volume relations," *Circulation*, vol. 95, pp. 2423-33, 1997.
6. G. Derumeaux, M. Ovize, J. Loufoua, X. Andre-Fouet, Y. Minaire, A. Cribier, and B. Letac, "Doppler tissue imaging quantitates regional wall motion during myocardial ischemia and reperfusion," *Circulation*, vol. 97, pp. 1970-7, 1998.
7. N. Yamazaki, Y. Mine, and A. Sano, "Analysis of ventricular wall motion using color-coded tissue Doppler imaging system." *Jpn J Appl Phys*, vol. 33, pp. 3141-3146., 1994.

8. A. Heimdal, A. Stoylen, H. Torp, and T. Skjaerpe, "Real-time strain rate imaging of the left ventricle by ultrasound," *J Am Soc Echocardiogr*, vol. 11, pp. 1013-9, 1998.
9. S. Urheim, T. Edvardsen, H. Torp, B. Angelsen, and O. A. Smiseth, "Myocardial strain by Doppler echocardiography. Validation of a new method to quantify regional myocardial function," *Circulation*, vol. 102, pp. 1158-64, 2000.
10. J. D'hoodge, A. Heimdal, F. Jamal, T. Kukulski, B. Bijnens, F. Rademakers, L. Halte, P. Suetens, and G. R. Sutherland, "Reginal Strain and Strain Rate Measurements by Cardiac Ultrasound: Principles, Implementation and Limitations.," *Eur J. Echocardiography*, vol. 1, pp. 154-170, 2000.
11. J. D'hoodge, F. Jamal, T. Kukulski, M. Kovalski, A. Heimdal, J. Thoen, P. Suetens, and B. Rademakers, "Calculation of strain values from strain rate curves: how should this be done?," *European Heart Journal*, vol. 21, pp. 335, 2000.
12. H. Kanai, H. Hasegawa, N. Chubachi, Y. Koiwa, and M. Tanaka, "Noninvasive evaluation of local myocardial thickening and ists color-coded imaging.," *IEEE Trans. on Ultrasonics, Ferroelectrics, and Freq Control.*, vol. 44, pp. 752-768, 1997.
13. A. Heimdal, "Doppler based ultrasound imaging methods for noninvasive asessment of tissue viability.," . Norway: Norwegian University of Science and Technology, 1999.
14. A. D. Fleming, W. N. McDicken, G. R. Sutherland, and P. R. Hoskins, "Assessment of colour Doppler tissue imaging using test-phantoms," *Ultrasound Med Biol*, vol. 20, pp. 937-51, 1994.
15. M. Uematsu, K. Miyatake, N. Tanaka, H. Matsuda, A. Sano, N. Yamazaki, M. Hirama, and M. Yamagishi, "Myocardial velocity gradient as a new indicator of regional left ventricular contraction: detection by a two-dimensional tissue Doppler imaging technique," *J Am Coll Cardiol*, vol. 26, pp. 217-23, 1995.
16. J. U. Voigt, M. F. Arnold, M. Karlsson, L. Hubbert, T. Kukulski, L. Hatle, and G. R. Sutherland, "Assessment of regional longitudinal myocardial strain rate derived from doppler myocardial imaging indexes in normal and infarcted myocardium," *J Am Soc Echocardiogr*, vol. 13, pp. 588-98, 2000.
17. L. Hatle and G. R. Sutherland, "Regional myocardial function--a new approach," *Eur Heart J*, vol. 21, pp. 1337-57, 2000.
18. T. Luopas, M. W.N., and A. P.L., "An Adaptive Weithted Median Filter for Speckle Suppresion in Medical Ultrasonic Images," *IEEE Trans on Circ Syst*, vol. 36, pp. 129-135, 1989.
19. C. H. Reinsch, "Smoothing by Spline Functions," *Num. Math.*, vol. 10, pp. 177-183, 1967.
20. C. De Boor, *A practical guide to splines*. New Yorl: Springer-Verlag, 1978.
21. M. Unser, A. Aldroubi, and M. Eden, "B-Spline Signal Processing: Part I--Theory," *IEEE Transactions on Signal rocessing*, vol. 41, pp. 821-833, 1993.